Nano-Micro Letters

Supporting Information for

Precise Thermoplastic Forming of Graphene Oxide Layered Solid by Polymer Intercalation

Zeshen Li[1], Fan Guo[1,2], Kai Pang[1], Jiahao Lin[1], Qiang Gao[3], Yance Chen[1], Dan Chang[1], Ya Wang[1], Senping Liu[1], Yi Han[4], Yingjun Liu[1], Zhen Xu[1*], Chao Gao[1*]*

[1]MOE Key Laboratory of Macromolecular Synthesis and Functionalization, Department of Polymer Science and Engineering, Key Laboratory of Adsorption and Separation Materials & Technologies of Zhejiang Province, Zhejiang University, 38 Zheda Road, Hangzhou 310027, P. R. China.

[2]National Special Superfine Powder Engineering Research Center, Nanjing University of Science and Technology, 1 Guanghua Road, Nanjing 210094, P. R. China.

[3]School of Mechanical Engineering, Southeast University, Nanjing, Jiangsu 211189, P. R. China.

[4]Hangzhou Gaoxi Technology Co. Ltd., Liangzhu, Yuhang District, Hangzhou, 311113, P. R. China.

* Corresponding author. E-mail: fanguo@njust.edu.cn; zhenxu@zju.edu.cn; chaogao@zju.edu.cn

Supplementary Figures

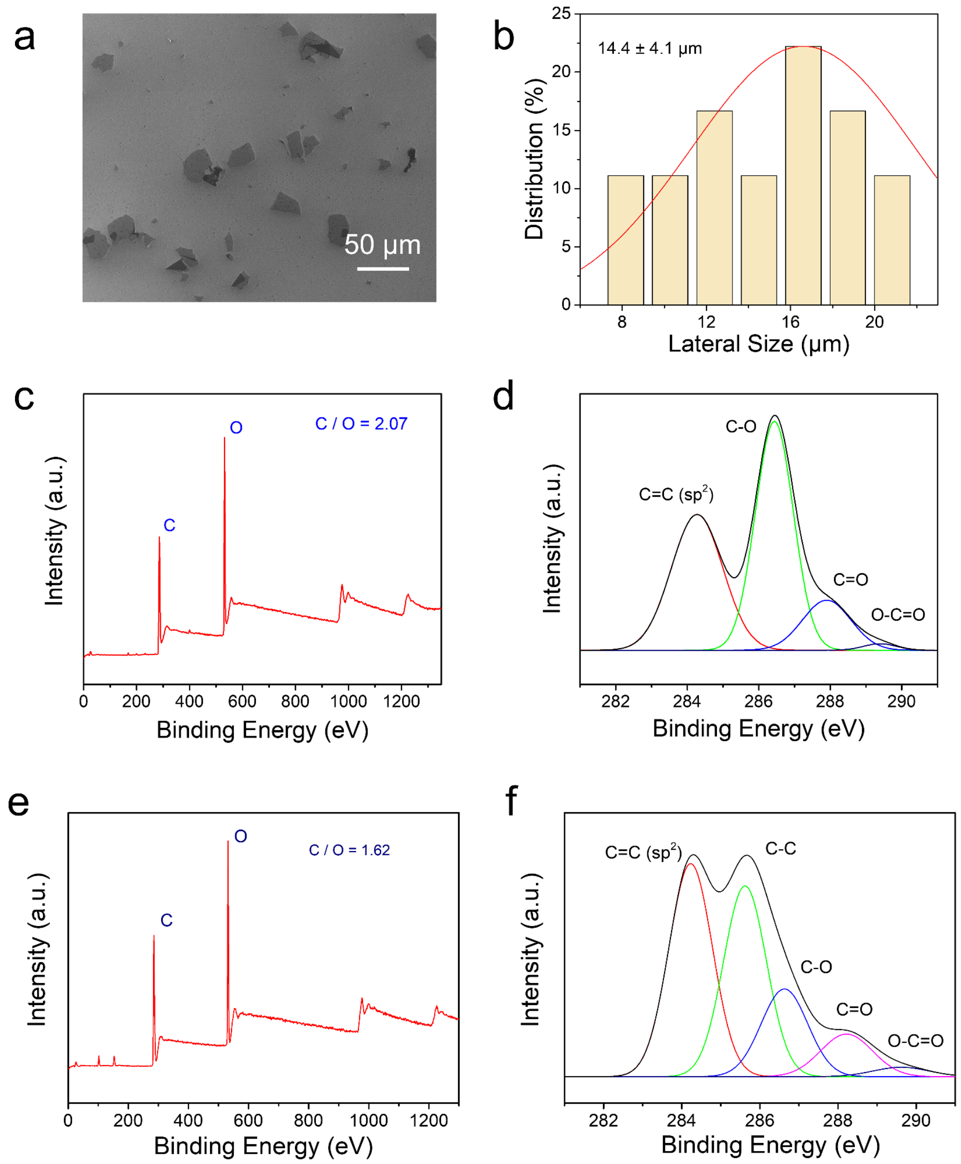

Fig. S1 Characterization data of GO sheets, GO film and Pi-GOS. (**a-b**) SEM images and size distribution of GO sheets with lateral size around 14.4 μm. (**c-d**) XPS spectra for full elements (**c**) and C1s (**d**) of GO film, divided into the four peaks: C=C skeleton and many oxygen-containing peaks (C-O, C=O and O-C=O). (**e-f**) XPS spectra for full elements (**e**) and C1s (**f**) of Pi-GOS (50% PVA), divided into the five peaks: C=C and C-C skeleton and many oxygen-containing peaks (C-O, C=O and O-C=O).

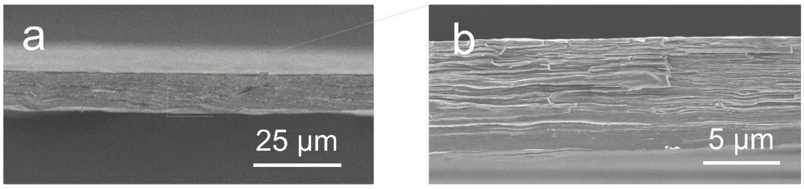

Fig. S2 The SEM images of Pi-GOS with lamellar structure.

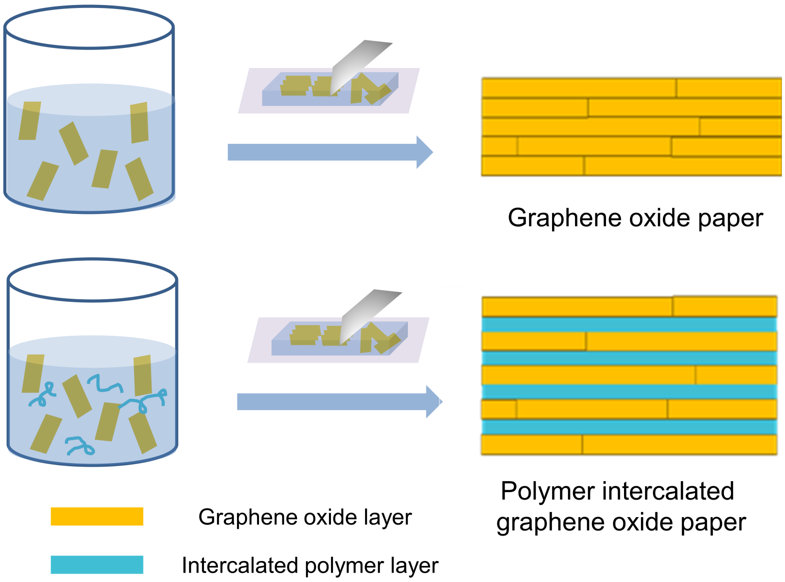

Fig. S3 The illustration of the polymer intercalating process and lamellar structures.

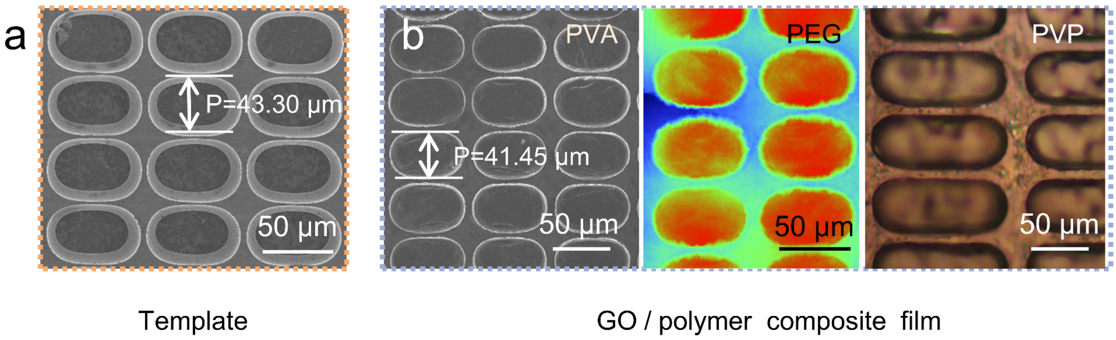

Fig. S4 Demonstration of the formability of Pi-GOS with different kinds of polymer. (**a**) SEM image of template. (**b-d**) The surface patterns on Pi-GOS composed of PVA (**b**), PEG (**c**) and PVP (**d**).

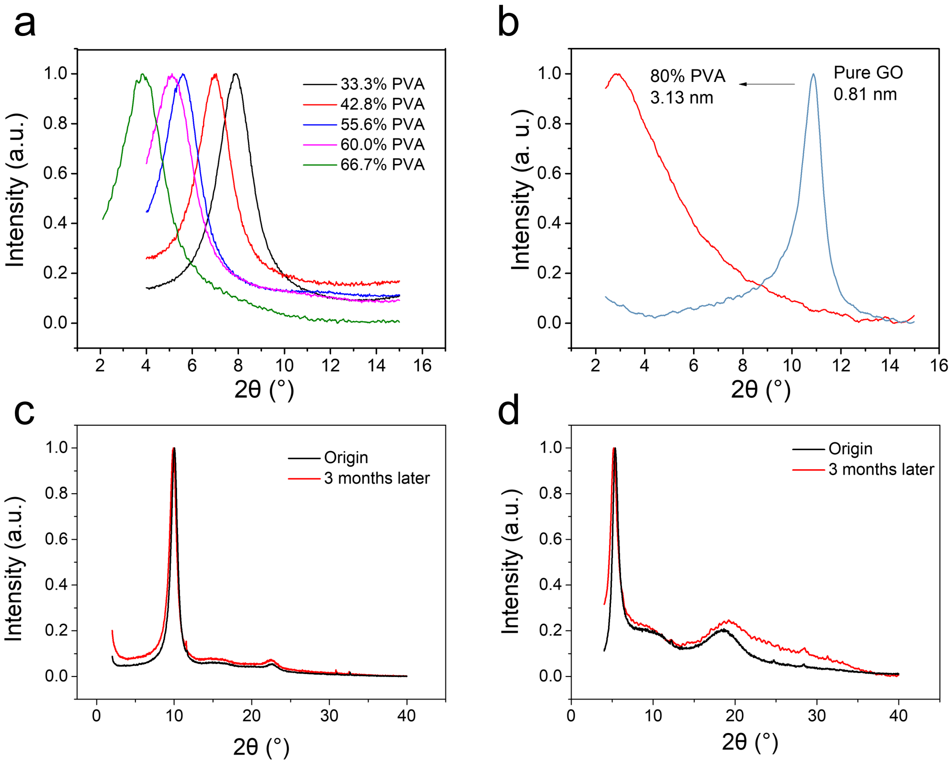

Fig. S5 XRD patterns of (a) Pi-GOS with different PVA contents, (b) the peak shift between pure GO film and composite film (80% PVA), (c) pure GO film and (d) Pi-GOS (50% PVA) now and after three months.

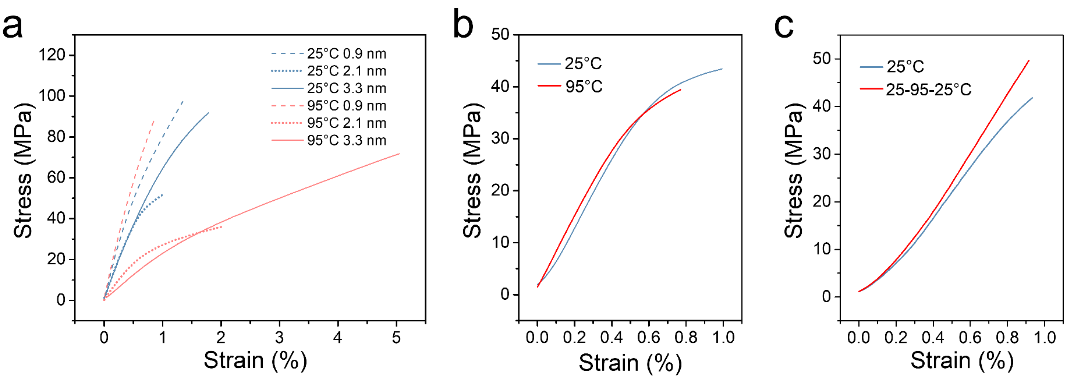

Fig. S6 Typical stress–strain curves of (**a**) Pi-GOS with different *d*-spacing, (**b**) pure GO film under different temperature and (**c**) Pi-GOS (d = 1.4 nm) under room temperature before and after annealing treatment.

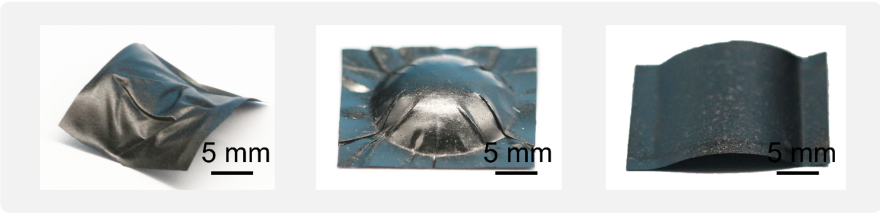

Fig. S7 The forming Pi-GOS with different Gauss curvatures.

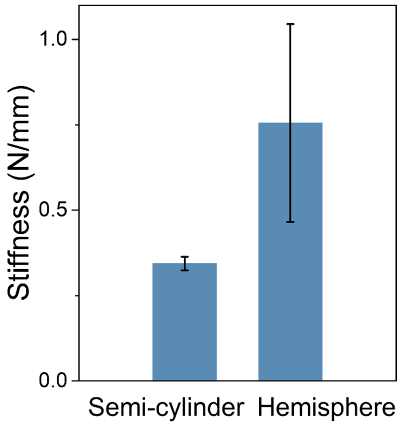

Fig. S8 Summary of stiffness of shells with different Gauss curvatures.

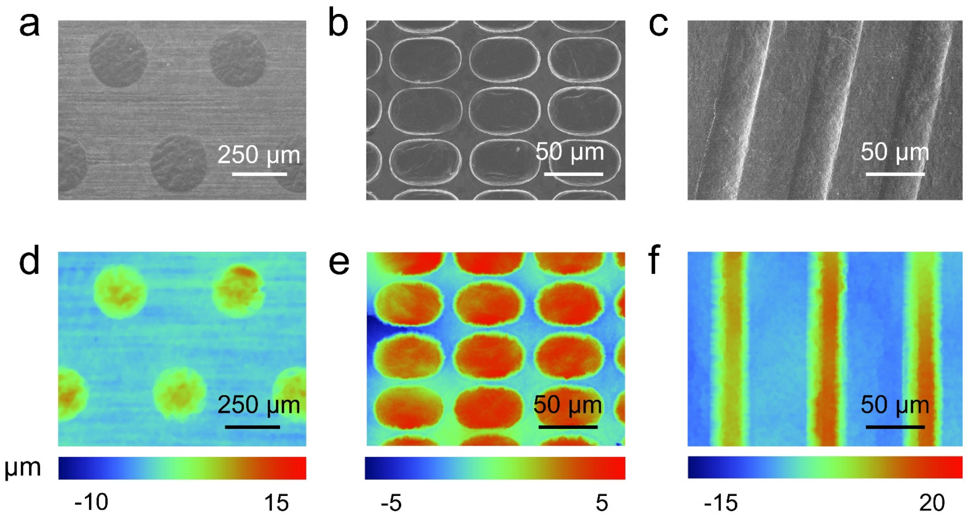

Fig. S9 Simple surface patterns on Pi-GOS through micro imprinting: (**a-c**) SEM images; (**d-f**) 3D-profile images.

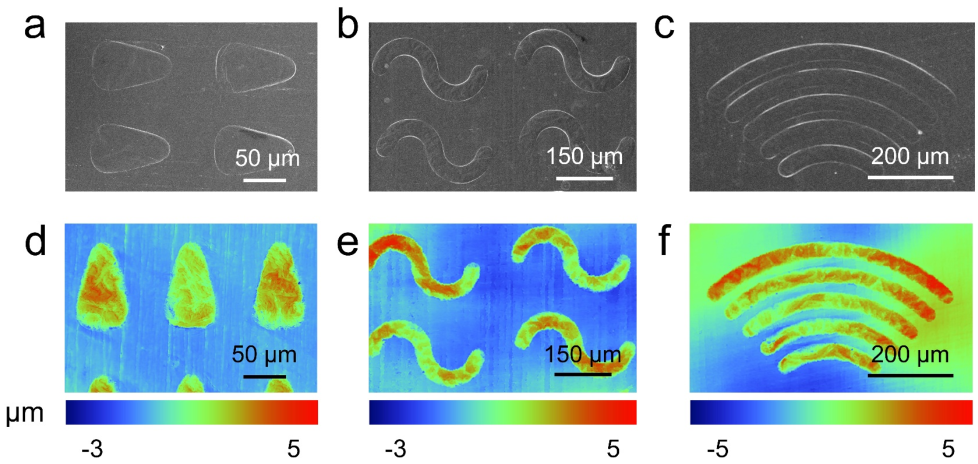

Fig. S10 Complex surface patterns on Pi-GOS through micro imprinting: (**a-c**) SEM images; (**d-f**) 3D-profile images.

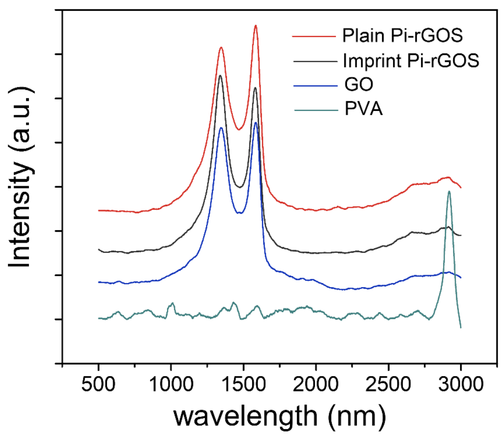

Fig. S11 Raman spectra of pure GO and PVA film and Pi-rGOS before and after imprinted.

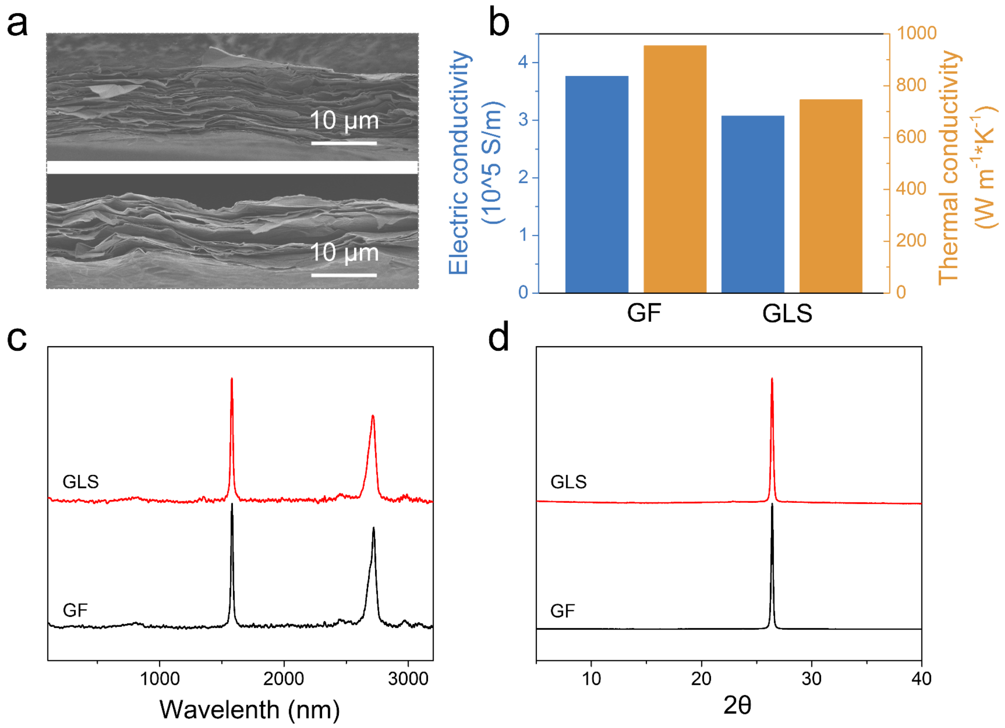

Fig. S12 Structure and properties characterization of GF and GLS. (**a**) The SEM images of GF (top) and GLS (bottom) with lamellar structure. (**b-d**) Electric and thermal conductivity (**b**), Raman spectrum (**c**) and XRD patterns (**d**) of GF and GLS.

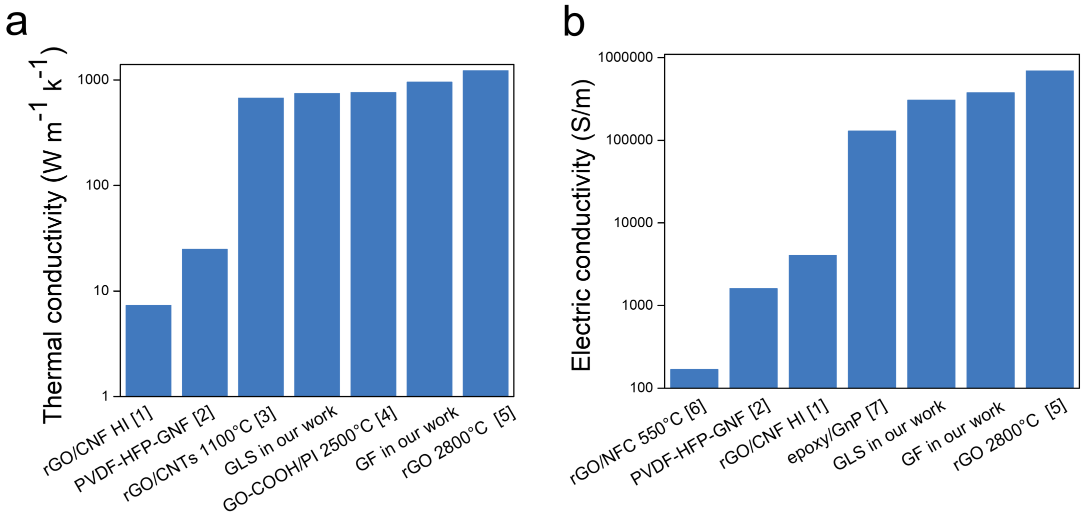

Fig. S13 Comparison of (**a**) thermal and (**b**) electric conductivity of our produced materials with other similar films in the literatures.

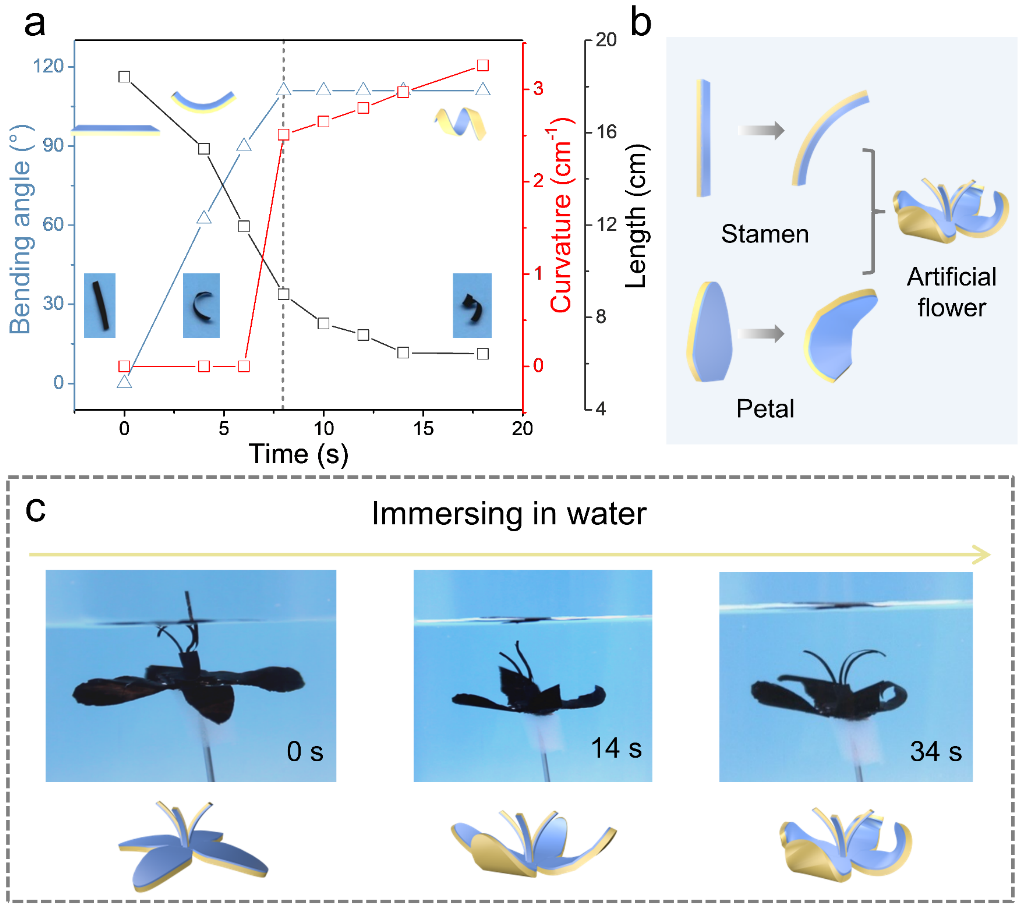

Fig. S14 The morphing behavior of Pi-rGOS. (**a**) Curves of bending angle, curvature and normalized length versus the immersing time. (**b-c**) Schematic illustration and digital images of the folding process of an artificial flower assembled from the imprinted Pi-rGOS immersing in water.

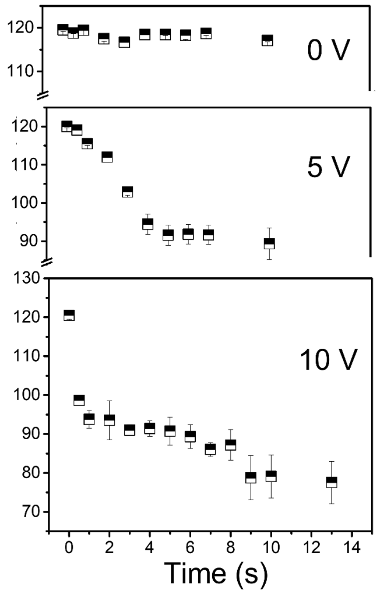

Fig. S15 Apparent contact angle variation of a water droplet on imprinted membrane with positive bias of 0, 5, and 10 V respectively.

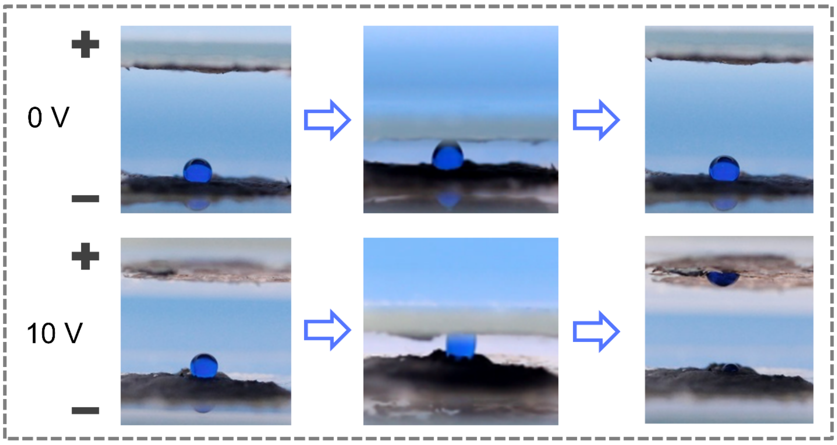

Fig. S16 Water droplet transportation response with imprinted membrane electrodes as both anode and cathode: without bias (top); the top film electrode as anode (bottom). The water droplet can be pumped from cathode to anode side by the effect of voltage while stays stable with no bias applied.

Supplementary References

[S1] W.X. Yang, Z.D. Zhao, K. Wu, R. Huang, T.Y. Liu et al., Ultrathin flexible reduced graphene oxide/cellulose nanofiber composite films with strongly anisotropic thermal conductivity and efficient electromagnetic interference shielding. J. Mater. Chem. C **5**, 3748--3756 (2017). https://doi.org/10.1039/C7TC00400A

[S2] A.A. Tarhini, A.R. Tehrani-Bagha, Graphene-based polymer composite films with enhanced mechanical properties and ultra-high in-plane thermal conductivity. Compos Sci Technol **184**, 107797 (2019). https://doi.org/10.1016/j.compscitech.2019.107797

[S3] G.J. Yuan, J.F. Xie, H.H. Li, B. Shan, X.X. Zhang et al., Thermally reduced graphene oxide/carbon nanotube composite films for thermal packaging applications. Materials **13**(2), 317 (2020). https://doi.org/10.3390/ma13020317

[S4] L.R. Ma, Y.X. Wang, X.D. Xu, Y.Y. Wang, C.G. Wang, Structural evolution and thermal conductivity of flexible graphite films prepared by carboxylic graphene/polyimide. Ceram. Int. **47**, 1076–1085 (2021). https://doi.org/10.1016/j.ceramint.2020.08.223

[S5] X.D. Zhang, Y. Guo, Y.J. Liu, Z. Li, W.Z. Fang et al., Ultrathick and highly thermally conductive graphene films by self-fusion. Carbon **167**, 249-255 (2020). https://doi.org/10.1016/j.carbon.2020.05.051

[S6] J.J. Chen, H.L. Li, L.H. Zhang, C. Du, T. Fang et al., Direct reduction of graphene oxide/nanofibrillated cellulose composite film and its electrical conductivity research. Sci. Rep. **10**, 3124 (2020). https://doi.org/10.1038/s41598-020-59918-z

[S7] Q.S. Meng, H. Wu, Z.H. Zhao, S. Araby, S.W. Lu et al., Free-standing, flexible, electrically conductive epoxy/graphene composite films. Compos. Part A **92**, 42–50 (2017). http://doi.org/10.1016/j.compositesa.2016.10.028